ADVANCED OPTICAL MATERIALS
www.advopticalmat.de

Dynamic Excitonic Beam Switching with Atomically-Thin Binary Blazed Gratings

Ludovica Guarneri, Thomas Bauer, Qitong Li, Jung-Hwan Song, Skyler Selvin, Ashley P. Saunders, Fang Liu, Mark L. Brongersma, and Jorik van de Groep**

Beam steering metasurfaces are ultra-compact optical coatings that offer on-demand redirection of optical power to specific diffraction orders. To achieve this, spatial gradients are commonly introduced in the phase of light scattered by plasmon or Mie resonant nanoparticles within the metasurface grating's unit cell. However, these phase gradients are oftentimes difficult to tune post-fabrication. Recently, excitons in monolayer 2D semiconductors have emerged as a new metasurface building block, due to their strong and electrically-tunable resonant light-matter interaction. These 2D excitonic metasurfaces offer the tantalizing prospect of beam switching within a single monolayer. Here, it is demonstrated how the 2D analog of binary blazed gratings enables such beam switching by mere nanopatterning of a large monolayer WS_2, even though nanoscale ribbons of WS_2 do not support geometrical resonances. By introducing a gradient in the nanoribbon width within the metasurface unit cell, an amplitude gradient combined with a small phase gradient in the scattered fields results in asymmetric diffraction efficiencies. Using a scattered-field analysis, it is shown that these gradients can be further engineered via interference effects with the substrate reflection. Finally, the electrical tunability of the exciton resonance is leveraged to achieve selective and dynamic beam switching with an atomically-thin metasurface.

1. Introduction

Dynamic metasurfaces play a crucial role in novel optoelectronic devices, where light manipulation and wavefront shaping in ultra-compact optical coatings are essential for applications including optical communication, augmented/virtual reality, and Lidar.[1] Beam steering is one of the most fundamental applications of metasurfaces, where light is selectively distributed to a specific diffractive order. Initial beam steering metasurfaces employed sub-wavelength arrays of plasmonic[2] or Mie-resonant[3] nanoparticles to engineer phase gradients within the metasurface unit cell. While such designs have developed into very efficient metasurfaces,[4] these demonstrations remained limited to passive beam steering.

To address this challenge, dynamic beam steering has been explored using metasurfaces embedded in liquid crystals,[5] by coupling plasmon or Mie resonances to materials that exhibit a tunable refractive index such as indium tin oxide[6] or phase change materials,[7] or by mechanical actuation.[8] More recently, exciton resonances in monolayer 2D transition-metal dichalcogenides (TMDs) have emerged as a new building block for metasurfaces with a tunable and strong light-matter interaction that is encoded in the material's optical response rather than the nanoscale geometrical design. This enables atomically-thin optical elements, in which the exciton resonance can be actively tuned through electrostatic gating.[9–12] This strong tunability was leveraged in a first demonstration of excitonic beam steering in a continuous $MoSe_2$ monolayer at cryogenic temperatures using nanoscale contacts to locally change the refractive index.[13] This raises the intriguing question of whether active beam steering can also be achieved by direct nanopatterning of a monolayer TMD, without the need for local electrodes and at room temperature. This prospect is particularly fascinating since it would enable dynamic beam steering in truly atomically-thin 2D excitonic metasurfaces, but requires new design rules to achieve phase gradients.

Here, we demonstrate how 2D binary blazed gratings enable both passive and dynamically selective beam switching in nanopatterned 2D excitonic metasurfaces. Despite the non-geometrical nature of the excitonic material's

L. Guarneri, T. Bauer, J. van de Groep
Van der Waals-Zeeman Institute
Institute of Physics
University of Amsterdam
Amsterdam 1098 XH, The Netherlands
E-mail: j.vandegroep@uva.nl
Q. Li, J.-H. Song, S. Selvin, M. L. Brongersma
Geballe Laboratory for Advanced Materials
Stanford University
Stanford, CA 94305, USA
E-mail: brongersma@stanford.edu
A. P. Saunders, F. Liu
Department of Chemistry
Stanford University
Stanford, CA 94305, USA

The ORCID identification number(s) for the author(s) of this article can be found under https://doi.org/10.1002/adom.202403257

DOI: 10.1002/adom.202403257

resonance, we find that the scattering phase is weakly affected by the nanoscale geometry of the metasurface building-blocks, due to polarization-dependent boundary conditions. We show that such size-dependence can be amplified via interference effects with the substrate reflection, offering a new opportunity to engineer both the local scattered phase and amplitude. Inspired by subwavelength binary blazed grating,[14] we design both a phase and an amplitude gradient across the period by progressively reducing the width of nanoribbons of WS_2 patterned onto a SiO_2 substrate. Here, we capitalize on the subtle scattering effects to obtain asymmetric diffraction in atomically-thin binary blazed gratings.

Via careful analysis of the scattered fields, we find that, while a phase contrast is essential to achieve asymmetric diffraction, the magnitude as well as the direction of such asymmetry are impacted in a non-intuitive manner by the amplitude contrast within the grating's period. In the regime where both amplitude and phase variations are subtle, the blazing efficiency strongly depends on the surrounding media, and can be optimized by engineering the dielectric environment (i.e., choice of substrate and superstrate). Based on these concepts, we experimentally show asymmetric diffraction in passive binary blazed grating structures, and furthermore demonstrate active and selective beam switching through electrostatic control of the exciton scattering amplitude, with the metasurface functionality fully encoded in the structured 2D monolayer material itself. Our results highlight the unconventional and novel opportunities offered by 2D excitonic metasurfaces for dynamic light manipulation and wavefront shaping.

2. Results

2.1. Concept of Beam Switching with an Atomically-Thin Interleaved Grating

Figure 1a illustrates our atomically-thin and active interleaved blazed grating enabled by exciton resonance tuning in monolayer (1L) WS_2. Upon normal incidence of light at resonant wavelengths, our design enables selective beam switching of reflected light solely by patterning a large-area monolayer of WS_2. The active aspect of the grating resides in the directional selectivity, which is achieved by suppressing the exciton resonance in selected parts of the material via electrostatic gating. The grating's baseline functionality builds on the established concepts of binary blazed gratings and graded-index gratings with a sub-wavelength period.[15] We transfer these ideas to a 2D metasurface, introducing the captivating novelty of post-fabrication tunability offered by the exciton resonance in the material.

Inspired by the work of Lalanne et al.,[14] we design a binary blazed grating directly in a monolayer of WS_2 on a quartz substrate, with sub-wavelength patterning within the unit cell. While conventional binary gratings maximize their efficiency by optimizing the nanoscale geometry in all three dimensions, we are limited to the two transverse dimensions and build our atomically-thin blazed grating by nanopatterning the monolayer. Figure 1b shows a schematic of the unit cell of the interleaved structure, made of two binary blazed gratings with opposite blazing vector. Each blazed grating has period $p = 2400$ nm and $N = 8$ subperiods of 300 nm in which the width of the 1L-WS_2 nano-ribbons (i.e., duty cycle) is gradually reduced (increased). The nanoribbon widths are: 275, 175, 100, 50, and 25 nm, with three empty subcells completing the grating period. The 2D geometry prohibits a significant accumulation of propagation phase, leaving only the scattered fields of the nanoribbons to tailor the local phase and amplitude. At the same time, the lack of propagation modes also relaxes the design rules: as long as all modes other than the 0th reflection are evanescent (i.e., subperiod $\frac{p}{N} < \frac{\lambda}{n_{sub}}$), the grating's subperiods behave like effective media with a dielectric constant governed by their duty cycle (i.e., the portion of WS_2 on substrate versus the portion of uncovered quartz).

The use of monolayer WS_2 for the proposed binary blazed grating is based on its strong light-matter interaction around the exciton resonance (λ~620 nm) as well as the robust tunability of the resonance via electrostatic doping. The former offers a significant refractive index contrast to the substrate and thus the opportunity to tailor the grating response via adjusting the duty cycle. The latter enables complete quenching of the resonant light-matter interaction.[9,16] To efficiently inject carriers into the monolayer and suppress its exciton resonance, we fabricate gold contacts and enclose the grating in an ionic liquid cell. We leverage this tunability to selectively direct where the reflected light is steered. While the unit cell of an individual binary blazed grating is asymmetric, interleaving it with a mirror copy of itself restores the overall symmetry and should thus yield symmetric diffraction. Although a similar effect could be achieved by placing the individual grating unit cells side by side (i.e., tiling instead of interleaving), this would reduce the overall efficiency of the grating. By quenching the exciton on one of the two blazed sub-gratings, a strong change in the material's susceptibility at resonance breaks the symmetry. This induces asymmetric diffraction and thereby beam switching. Using this principle, we demonstrate a three-state 2D metasurface that can redirect light either equally to $+1^{st}$ and -1^{st} diffraction orders (Figure 1d), or selectively promote either of them using a gate voltage (Figure 1c,e, see additionally Figure S1 (Supporting Information) for a wider spectral response outside of the dominant exciton resonance). In this configuration, the further allowed higher diffraction orders significantly decrease in efficiency per order (see Figure S2, Supporting Information) and are thus neglected in further discussion.

2.2. Grating Fabrication and Characterization

To verify this concept experimentally, we fabricate both single and interleaved blazed 1L-WS_2 gratings. We start from a high-quality and large-area monolayer of WS_2 directly exfoliated onto a SiO_2 substrate via the gold assisted exfoliation method.[17] To obtain the desired grating structure, we pattern the monolayer using electron-beam lithography and reactive ion etching. **Figure 2a** shows a microscope image of the interleaved structure. The grating has an active area of

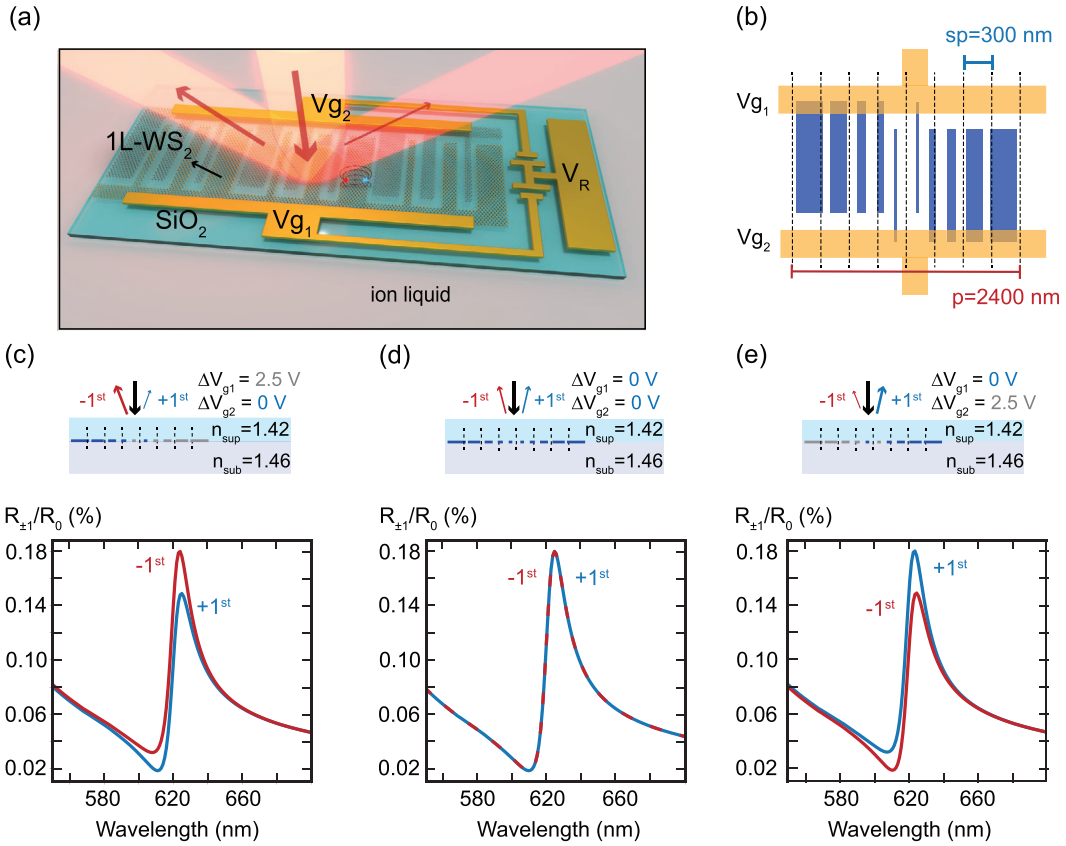

Figure 1. Dynamic excitonic beam switching in an atomically-thin WS_2 grating on SiO_2. a) Illustration of the concept: dynamic excitonic beam switching using an interleaved grating obtained by nanopatterning a large-area monolayer of WS_2 on SiO_2. Injecting electrons into one of the two sub-gratings via gold contacts suppresses its exciton resonance and introduces asymmetry. Under normal incidence more power is channeled to one of the two 1^{st} diffraction orders, resulting in preferential redirection of light. b) Schematic of a single period (p = 2400 nm) of the interleaved grating, composed of two mirrored blazed gratings with gradually reducing duty cycles in their subperiod (sp = 300 nm). c–e) Rigorous coupled wave analysis (RCWA) simulated diffraction efficiency in reflectance with the polarization parallel to the nanoribbons' length, of the $\pm 1^{st}$ diffraction orders normalized by the 0^{th} order. The grating is placed in an ionic liquid cell (refractive index of 1.42). For $V_R - V_{g1} = V_R - V_{g2} = 0$ V the grating is symmetric and equal power goes to the two 1^{st} diffraction orders (d). When electrons are injected into either of the two sub-gratings (applying a positive gate bias), the exciton resonance is suppressed in that sub-grating (gray in the schematics) and present in the other (navy blue in the schematics), and more power is channeled to either the -1^{st} (c) or $+1^{st}$ (e) diffraction order.

100 μm × 100 μm and is surrounded by a stripe of unpatterned 1L-WS_2 (in between the two white dashed lines). On each side of the grating, a gold contact is placed to inject carriers to the respective sub-grating. Figure 2b shows the topography of a portion of the grating (shaded red box in Figure 2a) measured via atomic force microscopy (AFM) prior to the removal of the poly-methyl-methacrylate (PMMA) resist used in the lithography step. The map reveals the successful patterning of the monolayer into the interleaved grating, although the two smallest features (25 and 50 nm ribbons in the unit cell) are absent due to underexposure in the lithography process (see Figure S3, Supporting Information for impact on diffraction efficiency). Across the same portion of sample, we also map the photoluminescence signal (PL) of the exciton resonance in 1L-WS_2, occurring around λ = 620 nm. The strong intensity contrast verifies the presence (and absence) of the monolayer (Figure 2c), confirming the successful patterning of the sample.

2.3. Passive Beam Switching Experiment with A Single Blazed Grating

We start by first investigating the case of a single, non-interleaved grating, before discussing the more complex active and interleaved structure. **Figure 3a** shows a microscope image of a single binary blazed grating that we fabricated on the same substrate (bottom), together with its unit cell geometry (top). On this grating, we perform passive measurements (no voltage applied) of the normalized diffraction efficiency – defined as $R_{\pm 1}/R_0$ – before assembling the ionic-liquid cell (i.e., superstrate is air). Figure 3b displays the reflectance of monolayer WS_2 on SiO_2 probed in the unpatterned area next to the grating. The spectrum shows a strong fingerprint of the exciton resonance ≈620 nm.[20]

Next, we measure the normalized diffraction efficiency of the 1^{st} diffraction orders in reflectance and normalize them to the 0th order (Figure 3c, see Section S3 (Supporting Information) for an error analysis of the diffraction efficiency). For each data

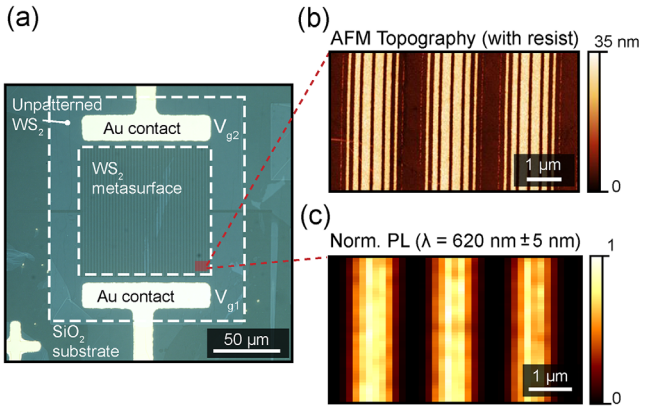

Figure 2. Fabrication of an atomically-thin interleaved blazed grating. a) Microscope image of the interleaved and blazed grating (100 μm × 100 μm) patterned into a large-area monolayer of WS_2 on a SiO_2 substrate. The white dashed lines highlight the grating contour (internal dashed line) and the surrounding area of unpatterned monolayer WS_2 (external dashed line). The two gold contacts are placed on either side of the grating to enable selective carrier injection into one of the sub-gratings. b) AFM topography of the grating prior removal of the resist (PMMA) for the area indicated by the red square in (a) showing the nanopattern of the grating across three unit cells. c) Spatially resolved map of the exciton PL (integrated over the range 620 nm ± 5 nm) for the same area as in (b), confirming the presence of monolayer WS_2 as well as the nanopattern of the grating. The PL variations within the unit cell are only partially visible due to the diffraction-limited collection area.

point, we use a confocal Nikon microscope equipped with a Bertrand lens. The latter allows us to image the back focal plane of the microscope objective and thus look at the diffraction orders in Fourier space. To scan the spectral range of interest (550–700 nm) we employ a tunable laser. A schematic of the setup is provided in Figure S4 (Supporting Information). Upon normal incidence illumination with an excitation wavelength around the exciton resonance, the efficiency of the $+1^{st}$ diffraction order is higher than the efficiency of the -1^{st} diffraction order, proving that a larger fraction of power is redirected to one preferential angle (i.e., $+1^{st}$ diffraction order). Note that the blazing in Figure 3c is achieved by merely nanopatterning the monolayer into nanoribbons that do not support geometrically-defined plasmon or Mie resonances in the visible spectral range (the common resonant building blocks for resonant metasurfaces) and neither relies on nanopatterned gate electrodes.[13] As such, the observed blazing constitutes an unprecedented demonstration of beam switching obtained in an atomically-thin design (0.6 nm thick).

2.4. Scattered Field Analysis

To unravel the mechanism that gives rise to asymmetric diffraction in atomically-thin binary blazed gratings, we start by analyzing the scattered fields of a single nanoribbon in a uniform dielectric environment with $n = 1$ (**Figure 4a**). The scattering cross section shows an increase in amplitude from σ_{scat} near-zero for $w = 25$ nm to a peak value close to 6 nm for $w = 275$ nm. The strong spectral peak at $\lambda \sim 620$ nm highlights that the scattering response of the monolayer nanoribbon is dominated by the exciton resonance and follows the material susceptibility χ, while the limit of $\sigma_{scat} < 10$ nm is a result of the atomic thickness of the material. Unlike conventional binary blazed gratings where the phase is controlled through the propagation phase, φ_{scat} is dominantly determined by the phase angle of χ, which is independent from the ribbon size as can be seen by the global shape of φ_{scat} for all ribbon widths in Figure 4a following the dispersion of $\varphi(\chi)$. This is based on the locally generated scattered fields being proportional to the polarization $P = \varepsilon_0 \chi E$ of the material.[9,18] Nevertheless, we observe a small ($\Delta\varphi_{scat} < 0.1$ rad) variation in the phase of the scattered fields (φ_{scat}) as a result of the nanoscale confinement of the fields on the nanoribbons (see Figure S5 (Supporting Information) for the spatial field profiles of the scattered fields of the individual nanoribbons). Figure 4a thus highlights that the ribbon width can be used to introduce a (small) phase gradient associated with an amplitude gradient within a grating's unit cell.

Using a discrete Fourier transform model (see methods for details), we can assess the individual role of the amplitude and phase gradients to explain the asymmetric diffraction observed in Figure 3c. Assuming a perfect amplitude gradient (A varies linearly from 0 to 1 within one unit cell) but no phase gradient yields a fully symmetric diffraction pattern (Figure 4b, red). The majority of the power remains in the 0th diffraction order and the remaining power is symmetrically distributed over the higher diffraction orders, with decreasing intensity for increasing order. As such, a pure amplitude gradient within the unit cell does give rise to diffraction, but strictly symmetric. A pure phase gradient on the other hand (Figure 4b, blue), where $A = 1$ throughout the unit cell and φ varies linearly from 0 to π, results in a strong asymmetry where $+1^{st}$ order is much stronger than the -1^{st} order – even larger than the 0th order. This general case study points out the necessity of a phase gradient to achieve asymmetric diffraction and provides us with the intuition that, in a mixed scenario where both amplitude and phase vary, the extent of both gradients determines the observed efficiencies of the diffraction orders.

2.5. Effective Reflection Coefficient of Sub-Diffractive Gratings

A crucial difference between the scattering-field analysis so far and the experiments in Figure 3 is the asymmetric dielectric environment where the atomically-thin layer is placed on a quartz substrate and features air as the superstrate. For atomically-thin layers that reflect only a few percent of the incident light, the scattered fields have a comparable amplitude to the reflected fields of the underlying SiO_2 substrate. The interference of these two contributions is key to describe the exciton line shape of continuous films,[18] and can be leveraged to further engineer the total scattered field. Building on the insight from a single nanoribbon, we assess the complex reflection coefficient r of a periodic (non-blazed) grating on a quartz substrate with sub-wavelength pitch $p = 300$ nm, equal to the sub-unit cell in Figures 1–3. In this scenario the reflection is limited to the 0^{th} order (no diffraction) and we explore the impact of the nanoribbon width on the effective reflection coefficient.

As highlighted in Figure 4, the scattered fields of the nanoribbons have an amplitude that varies with w, yet the phase is largely

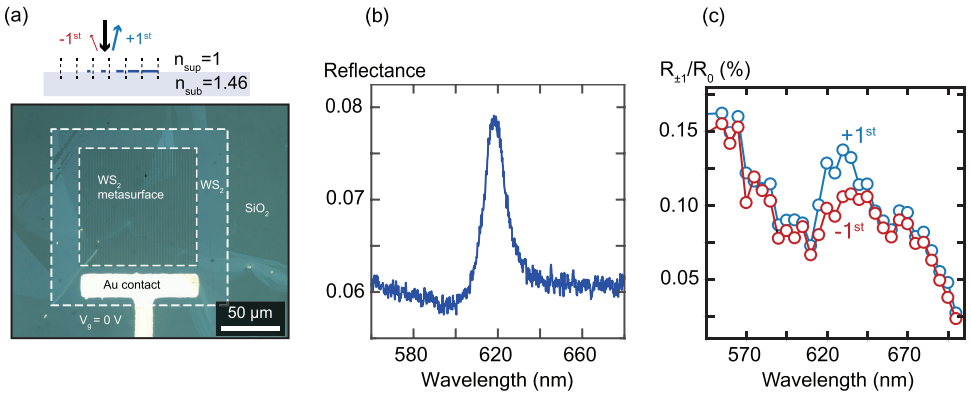

Figure 3. Single blazed grating passive measurements. a) Microscope image of the single blazed grating of monolayer WS_2 on a SiO_2 substrate with period p = 2400 nm and subperiod sp = 300 nm. The white dashed lines highlight the 100 μm-sized grating area (internal line) and the unpatterned monolayer (external line). An illustrative cross section of one period of the grating is also shown (top), with the arrows indicating the designed functionality when no voltage is applied. b) Reflectance spectrum of monolayer WS_2 on SiO_2 in air, measured in the unpatterned area between the two dashed lines. c) Experimental diffraction efficiency of the + 1^{st} (blue) and -1^{st} (red) orders in reflectance, normalized by the 0th diffraction order.

dictated by χ. The reflection coefficient of a free-standing grating ($w = 100$ nm, no substrate) will therefore trace out their dispersion in the second quadrant of the complex plane when λ is varied from 475 to 750 nm (**Figure 5a**, red). Whereas a semiconductor typically shows a gradual dispersion toward lower χ for increasing wavelengths (i.e., slow decrease in n and decrease in absorption), the exciton resonances trace out loops that are superimposed on this trend. From these loops, the amplitude (length of the vector from the origin) and the phase (angle of the vector with respect to the real axis) of r can be retrieved for each wavelength. The substrate reflection on the other hand, is fixed by the index mismatch with the superstrate and exhibits a phase angle of π radians. Interference of the nanoribbon scattering with the substrate reflection gives rise to a large offset in the -x-direction in the complex plane (Figure 5a, blue). We now also take into account a superstrate different from air, namely DEME:TFSI, as used in our active measurements performed inside an ionic liquid cell (Figure 1c–e). In this nearly index-matched situation, where $n_{sub} = 1.46$ and $n_{sup} = 1.42$ (as given by the manufacturer), the real part of the reflection coefficient shifts almost back toward the free-standing case (Figure 5a, black).

Next, we set $\lambda = 624$ nm, to the peak of the normalized diffraction efficiency, and increase w from 0 to 275 nm, which corresponds to scanning the duty cycle of the grating from 0% to 92%. Figure 5b shows r in the complex plane for a free-floating grating (reds), a grating on SiO_2 in air (blues), and a grating on SiO_2 covered by ionic liquid (grays). For the free-standing grating, the vectors show a very small variation in the phase angle. For the on-substrate and ionic liquid scenarios on the other hand, the interference with the substrate reflection results in a distinct variation in phase angle –, i.e., the scattered fields from 2D materials with an exciton resonance show a phase angle with respect to the reflection from bare SiO_2 (see $\Delta\varphi_r$ in Figure 5b), associated with the increase in amplitude.

We retrieve the contrast in amplitude offered by the grating with respect to a bare substrate $\Delta|r| = r(w) - r(w = 0)$ (Figure 5c),

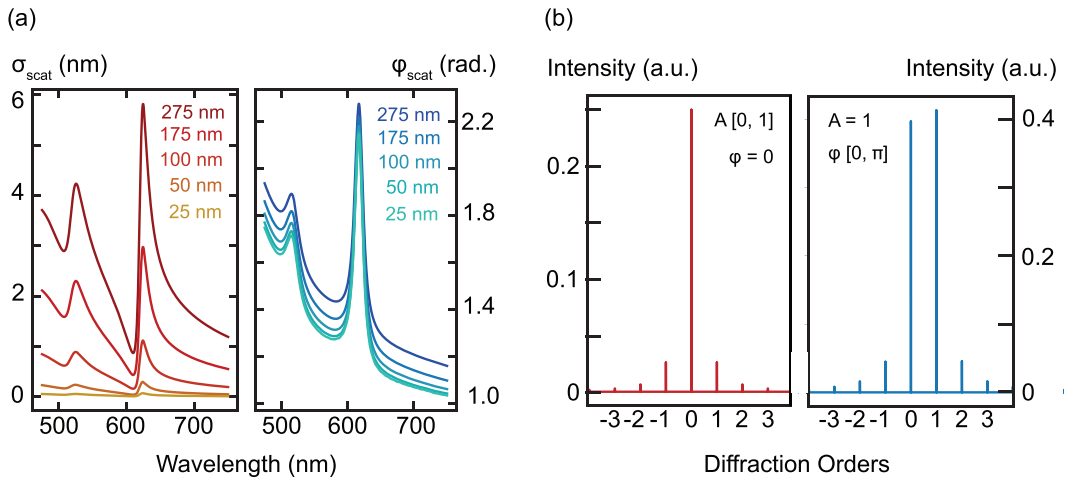

Figure 4. Scattered field analysis of a free-floating grating and general FFT calculations. a) Scattering cross section (left panel, reds) and scattering phase (right panel, blues) of free-standing ribbons of WS_2 with widths ranging from 25 to 275 nm. b) Calculated diffraction intensities for a pure amplitude grating (left panel in red, A ranges from 0 to 1 and $\varphi = 0$) and pure phase grating (right panel in blue, φ ranges from 0 to π and A = 1).

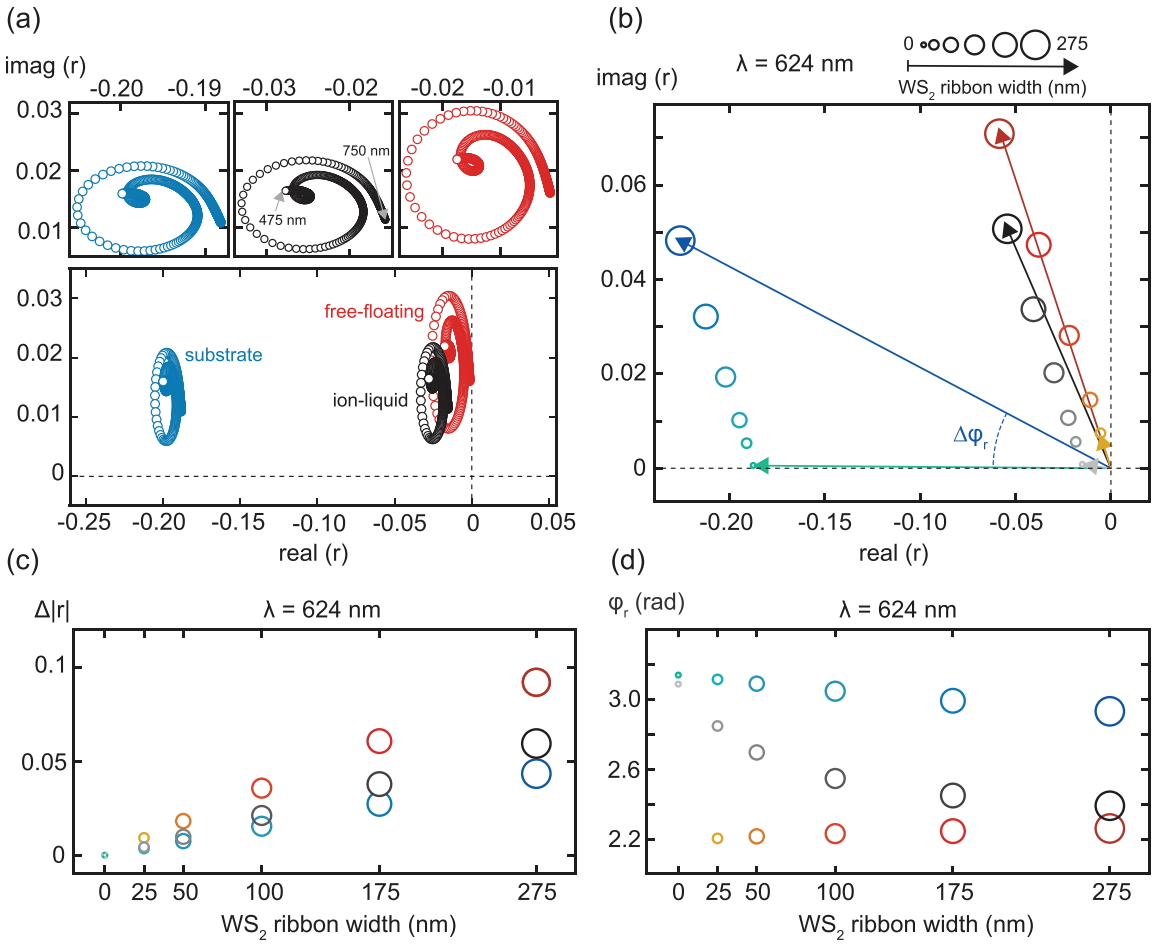

Figure 5. Simulations of the effective reflection coefficient. a) r in the complex plane for a 1L-WS_2 ribbon with w = 100 nm for the cases of free-standing (red), on substrate (blue), and covered by ionic liquid (black) gratings. The top panels offer a zoomed view of the three cases. b) r in the complex plane for varying w and for the same three color-coded scenarios ($\lambda = 624$ nm): free-standing (reds), on substrate (blues), and on substrate covered by ionic liquid (grays). The marker sizes are proportional to the ribbon widths and range from 0 nm (on substrate) to 275 nm. A representative phase angle with respect to bare SiO_2 (i.e., $\Delta\varphi_r$) is indicated for the blue vector. c) Amplitude contrast with respect to the bare substrate $\Delta|r| = r(w) - r(w = 0)$ and d) phase of r (φ_r) for increasing width for $\lambda = 624$ nm. Colors and sizes of the markers have the same meaning as in (b).

and the phase angle of *r* (Figure 5d). The amplitude contrast is of the same order of magnitude for all three cases, with the free-standing grating showing the largest range of amplitudes (proportional to the scattering cross section). We define the phase contrast as the difference between the phase of the largest ribbon and that of the smallest one ($\Delta\varphi_r = \varphi_r(w = 275\text{ nm}) - \varphi_r(w = 25\text{ nm})$) and find that, between the three studied scenarios, the phase contrast varies more significantly than the amplitude. While the free-standing grating offers a small positive phase gradient (0.057 radians), mixing the nanoribbon scattering with the reflection of a SiO_2 substrate significantly changes the phase contrast to −0.183 radians. Finally, by covering the substrate with ionic liquid, the range in phase angles is further enhanced to −0.457 radians, 8 times larger than for the free-standing grating. Delicate engineering of the substrate reflection thus provides an additional degree of freedom to control the scattering amplitude and phase of sub-wavelength unit cells.

2.6. Asymmetric First-Order Diffraction Efficiency

Building on the extracted phase and amplitudes from Figure 5c,d, we now aim to evaluate the asymmetric diffraction efficiencies using the discrete Fourier transform model. **Figure 6a** shows the result for the free-floating grating. Despite the very small phase gradient, the grating yields asymmetric diffraction, with more intensity directed to $+1^{st}$ diffraction order. The asymmetry is additionally confirmed by the FDTD-simulated normalized diffraction efficiency spectrum of $+1^{st}$ and -1^{st} orders (Figure 6b), where the sharp peak at 600 nm originates from a Wood's anomaly.[22] It is worth highlighting the good agreement obtained between Figure 6a,b despite using different methods. While the amplitudes and phases employed in the Fourier model (Figure 6a) are extracted from a periodic, yet non-blazed scenario, the FDTD simulations employ the complete as-designed blazed unit cell. The efficiency spectra and FFT-analysis for the single blazed grating on quartz, both in air as well as in ionic liquid,

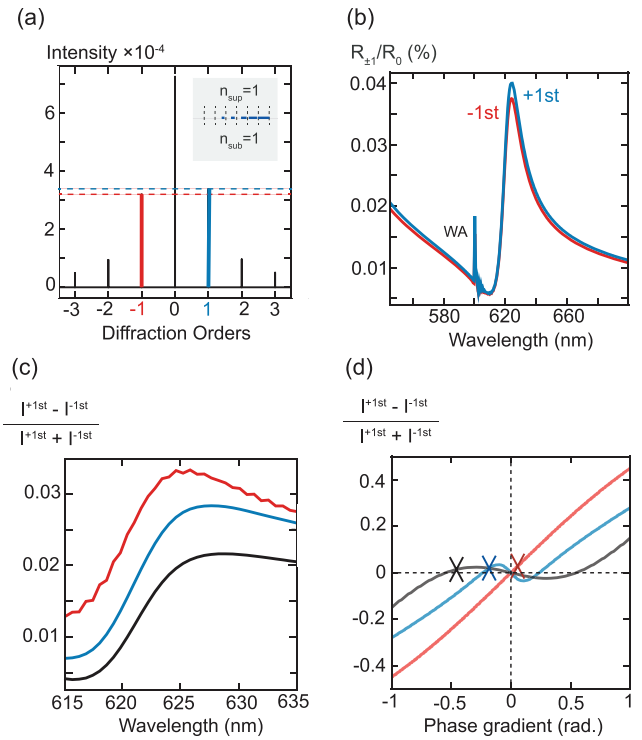

Figure 6. Asymmetric first-order diffraction efficiency. a) Fourier model calculated intensity distribution of the first three diffraction orders for the free-floating blazed grating for $\lambda = 624$ nm. b) FDTD-simulated first order normalized diffraction efficiency of $+1^{st}$ and -1^{st} diffraction orders around the exciton resonance (WA: Wood's anomaly). c) Degree of asymmetry around resonance for the free-floating (red), substrate/air (blue), and substrate/ionic liquid (black) case. d) Degree of asymmetry for the same gratings at $\lambda = 624$ nm while artificially varying the phase contrast of the period in the range [−1,+1] radians.

can be found in Figure S6 (Supporting Information) for comparison.

To better compare the asymmetric diffraction of the free-standing grating to those on substrate, we define the degree of asymmetry as $(I^{+1^{st}} - I^{-1^{st}})/(I^{+1^{st}} + I^{-1^{st}})$. Figure 6c shows the trends of the asymmetry around resonance for the free-floating (red), substrate/air (blue), and substrate/ionic liquid (black) gratings. Multiple points can be observed from this analysis. First, offering a coupled control over both amplitude and phase of the scattered light, all three scenarios lead to asymmetric diffraction. Second, despite the opposite sign of the phase gradient for the free-floating case, the direction of the asymmetry is identical in all three cases. Third, the free-floating grating surprisingly displays a larger degree of asymmetry than the other two cases, despite the much smaller phase contrast.

To explain these results, we start from the insight that a phase gradient across the grating period is essential to observe blazing (Figure 4b). We again use the Fourier model, set the wavelength to 624 nm where the asymmetry is maximized, and keep the amplitudes of each subperiod fixed to the values extracted from Figure 5c. Next, we calculate the degree of asymmetry as we artificially vary the phase gradient within the period between −1 and +1 radians (Figure 6d). The three markers highlight the phase gradients extracted from Figure 5d for the three investigated scenarios.

When the phase gradient is 0 (i.e., pure amplitude grating), all three curves cross the symmetry point and the diffraction is fully symmetric. However, the three different combinations of amplitude and phase gradients yield strikingly different trends. For the free-floating grating, the small positive phase gradient indicated by the dark red marker is associated with a positive degree of asymmetry, in agreement with the directionality observed in Figure 6a–c. Also, the degree of asymmetry scales monotonically with the phase gradient, showing a change in directionality for negative gradients.

In contrast, the substrate/air (blue) and substrate/ionic liquid (black) curves present an intriguing S-shaped trend and cross the symmetry point three times, revealing three sign switches within the studied range of phase gradients. The navy blue and black markers both are on the negative phase gradient side, however their degree of asymmetry lands on the small portion of the curve that rises above zero. This explains why the direction of the asymmetry coincides with that of the free-floating grating, despite the opposite phase gradient sign. The direction and the magnitude of the asymmetry are therefore strictly associated with both phase and amplitude gradients across the unit cell, that must therefore be evaluated jointly. Moreover, the observed asymmetric diffraction not only depends on the grating's blazed duty cycles and ribbon material, but also on the substrate and superstrate material, highlighting how proper engineering of the dielectric environment is crucial to optimize the optical performance of the grating.[18] The S-shaped trend is thus a direct response of the interference between this dielectric environment response and an equally strong material-based grating response.

2.7. Active Beam Switching in an Interleaved Blazed Grating

Finally, we focus on the active measurements. **Figure** 7a shows the interleaved and blazed 1L-WS_2/SiO_2 grating just before the fabrication of the ionic liquid cell. First, to verify the functioning of the electrochemical cell as well as the tunability of the exciton resonance, we measure the gate dependence of the reflectance spectrum of the unpatterned area near contact 1 (Figure 7b). For $V_{g1} = 0$ V, we see a clear fingerprint of the exciton resonance, this time with a slightly different spectral shape as compared to Figure 2b due to the different dielectric environment ($n_{sup} = 1.42$).[18] For $V_{g1} = 2.5$ V the exciton resonance is suppressed through screening, exciton-electron scattering, and trion formation.[16,19] A fingerprint of these charged quasi-particles is visible as a small peak at $\lambda \sim 650$ nm (Figure 7b, gray) red-shifted with respect to the neutral exciton. The measured spectra confirm that we are able to suppress the exciton resonance in the monolayer via V_{g1} and thus induce a large change in the refractive index of one sub-grating while leaving the other one unchanged.

After verifying the tunability of the exciton in our device, we move on to investigate the effect of electrostatic doping on the efficiency of the grating. When $V_{g1} = 0$ V (Figure 7c), the exciton resonance is present on the whole structure. The design is composed of two oppositely-oriented blazed gratings with the same, yet mirrored, optical response. The blazing-effect of the two individual halves cancels out, yielding a symmetric diffraction

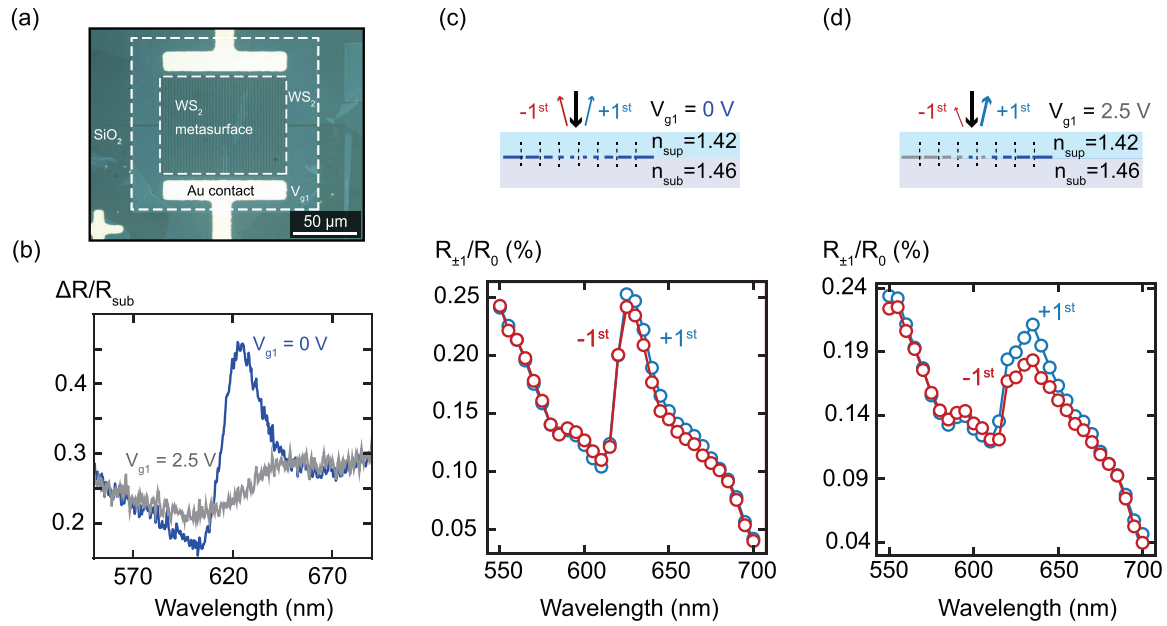

Figure 7. Active beam switching measurements in an interleaved grating. a) Microscope image of the interleaved grating before fabrication of the ionic liquid cell. Carrier injection is only possible via the bottom contact (V_{g1}0 V) due to an interrupted contact-to-pad line for the top contact. b) Differential reflectance spectra $\Delta R/R_{sub} = R_{WS_2} - R_{SiO_2}/R_{SiO_2}$ in the neutral state (V_{g1} = 0 V, blue) and upon electrostatic doping (V_{g1} = 2.5 V, gray) when the exciton is suppressed. Spectra are measured in the unpatterned region near contact 1. c,d) Experimental diffraction efficiency of $+1^{st}$ (blue) and -1^{st} (red) diffraction orders normalized to the 0th order and measured in reflectance, showing symmetric diffraction for V_{g1} = 0 V (c) and asymmetric diffraction for V_{g1} = 2.5 V (d).

response, where both $\pm1^{st}$ diffraction orders receive the same optical power. Indeed, the measured normalized diffraction efficiency spectra overlap, showing only very small differences that we attribute to experimental noise. When $V_{g1} = 2.5$ V (Figure 7d), the bottom sub-grating has a lower refractive index due to the suppression of the exciton resonance, reducing its optical contrast across the period. As a result, the blaze effect of the top sub-grating dominates the response of the overall structure, and we retrieve the asymmetric behavior with $+1^{st}$ diffraction order revealing a larger efficiency around resonance. Note that the two experimental results in Figure 7c,d show good agreement with the simulations (Figure 1d,e). Due to an interrupted contact-to-pad line for contact 2, it was not possible to experimentally verify the third state of the metasurface corresponding to Figure 1d (i.e., more power redirected to the -1^{st} order for $V_{g2} = 2.5$ V and $V_{g1} = 0$ V).

3. Discussion

In summary, our results demonstrate active and selective redirection of light in an atomically-thin 2D metasurface, obtained via the synergic use of sub-wavelength patterning of a monolayer of WS_2 and the tunability of its exciton resonances. Unlike established beam-steering metasurfaces, the grating's 2D scattering elements do not support geometry-dependent plasmon or Mie resonances, nor facilitate the accumulation of a propagation phase. Instead, the blazed grating operation relies on the strong excitonic light scattering of the monolayer WS_2 nanoribbons, which renders a nanopattern-dependent optical response (i.e., dependent on the duty cycle in each subperiod). By leveraging the interference of the nanoribbon scattered fields with the few-percent reflectivity of the SiO_2 substrate, we demonstrate additional engineering of the local phase and amplitude, beyond the small range of phase angles that can be achieved with free-floating nanoribbons. We note that this concept of amplitude and phase engineering through interference with the substrate reflectance is not limited to monolayer TMDs and can be easily generalized to other non-resonant scattering particles that exhibit a scattering amplitude that is roughly matched by the reflection of the underlying substrate.

Intriguingly, we find that a larger phase contrast does not necessarily imply an enhancement of the asymmetry response for a given amplitude gradient. While the phase contrast across the period is imperative to achieve asymmetric diffraction, the amplitude variation also directly impacts the blazing efficiency (i.e., degree of asymmetry). Their relative contributions show non-intuitive trends that depend on the combination of substrate and superstrate, highlighting the importance of a careful choice of the dielectric environment to maximize the blazing efficiency.

Crucially, our design combines nanopatterned 2D monolayers with electrostatic suppression of the exciton resonance to achieve active control over the blazing direction at room temperature. Such active tuning of the scattering response of nanoscale structures is unique to 2D TMDs and enables electrically-induced asymmetries in an otherwise fully symmetric structure, without the need for local nanoscale electrical contacts. In absolute terms, the atomic length scale of the light-matter interaction fundamentally limits the diffraction efficiencies[20] and the small

phase gradient within the unit cell offered by the monolayer nanoribbons limits blazing of the diffraction to few percent. While cryogenic operation of 2D excitonic metasurfaces increases the material's quantum yield and oscillator strength[21] and thereby their optical efficiencies,[22] as well as reduces the excitonic linewidth, room-temperature operation with increased efficiencies could be achieved by employing 2D material superlattices[23] that would enable stronger light-matter interactions and larger phase gradients. Finally, we note that the use of ionic liquids for the gating of our monolayer devices offers facile tuning of the optical response over large areas but limits the switching speeds to the millisecond range due to the high mass of the moving ions. For potential applications, it would be more desirable to employ solid-state gating schemes instead which enable high-speed modulation of the carrier density at the cost of more complex device designs. Overall, our results highlight how the tunable and strong light-matter interaction in 2D excitonic metasurfaces enable new routes toward dynamic wavefront manipulation in atomically-thin optical elements.

4. Experimental Section

Large-Area Exfoliation: Monolayer WS_2 was exfoliated onto a quartz substrate from bulk WS_2 single crystals (HQ Graphene) using a gold-tape exfoliation technique.[17] In this method, a 100 nm gold layer was first deposited onto a clean Si wafer (Nova Wafers) via thermal evaporation and subsequently coated with polyvinylpyrrolidone (PVP) to prevent contamination. A piece of thermal release tape (Nitto, RA95LS) was then used to lift the Au layer from the Si substrate. The exposed gold surface was immediately brought into contact with a freshly cleaved WS_2 crystal, allowing the monolayer to adhere to the Au surface. The resulting stack, composed of thermal release tape, PVP, Au, and the WS_2 monolayer, was transferred onto a quartz substrate. Heating was applied to remove the thermal release tape, and the PVP layer was dissolved in water. The gold layer was etched away using a mild gold etchant solution (KI/I_2), which selectively removed the Au without affecting the WS_2 monolayer. Finally, the sample was rinsed with water and isopropanol to obtain a clean WS_2 monolayer on the quartz substrate.

Sample Fabrication: The process was started by fabricating markers and contacts using UV-lithography. 2 µm of negative-tone resist (ma-N 1420) was spin-coated and the sample was exposed to UV-light with a dose of 450 mJ cm^{-2} using a custom-made film UV mask (JD Photodata). After development (ma-D 533/S, 65 s), 100 nm of Au was evaporated (via a Polyteknik Flextura M508 E) on top of 3 nm of Cr used to enhance adhesion and conclude the step by lift-off in Acetone. Next, 80 nm of polymethylmethacrylate (PMMA 950K A8, further diluted by 1:7) was spin-coated to serve as a positive-tone electron-beam resist layer. A thin conductive polymer layer (E-Spacer Electra 92) was further spin-coated to mitigate charging effects during the electron-beam lithography exposure (using a Raith Voyager 50 kV system, electron-beam current = 125 pA, dose = 280 µC cm^{-2}). After rinsing off the Electra 92 for 20 s in water and development in a MIBK:IPA 1:3 solution for 45 s followed by a rinse in IPA, argon plasma etching (Oxford PlasmaPro 80) was performed with RF power = 50 W for 10 s to selectively etch the WS_2 monolayer. The remaining resist was subsequently removed by warm acetone. Next, a second round of UV lithography was performed to isolate the grating. Hexamethyldisilazane (HMDS) was initially applied to the sample as a primer for the photoresist. A positive-tone photoresist (MEGAPOSIT SPR 3612) with a thickness of ≈1.5 µm was then spin-coated. Optical lithography was performed using the Heidelberg MLA 150 with a dose of 80 mJ cm^{-2}, followed by the development in MEGAPOSIT MF-26A for 40 s. Finally, a second-round argon plasma etching with the same recipe was conducted to remove the exposed WS_2 monolayer region. The remaining photoresist was stripped in acetone.

Ionic Liquid Cell Fabrication: An optically-transparent electrochemical cell was fabricated on top of the gratings. A pair of ∼2 mm-wide strips of thermoplastic (∼60 µm thick, Solaronix Meltonix 1170–60) was placed along the sides of the sample, and a cover glass was placed on top (type no. 1). Heating the thermoplastic to 130 °C on a hot plate sealed the cover glass in place, creating an open channel. Finally, the cell was filled with DEME:TFSI ionic liquid (Diethylmethyl(2-methoxyethyl)ammonium bis(trifluoromethylsulfonyl)imide, Sigma–Aldrich), and sealed the two openings using epoxy.

Photoluminescence Map: The photoluminescence (PL) map (Figure 2) was performed in a Witec α300R confocal raman microscope with a 532 nm fiber-coupled diode laser as an excitation source. A 100 × Zeiss EC Epiplan-Neofluar (NA = 0.9) microscope objective was used to collect from a diffraction-limited area on the sample. The studied sample area was scanned by means of an x-y piezo stage, with 100 nm step size. A photonic-crystal fiber (7 µm effective core diameter) was used to send the collected signal to a Witec UHTS300 SMFC VIS spectrograph (600 lines/mm grating for PL) coupled to a Andor Newton EMCCD camera cooled to −60 °C to suppress electronic noise.

Atomic Force Microscope Topography: AFM measurements (Figure 2) were performed using a Bruker Dimension Fastscan in tapping mode equipped with a SCANASYST-AIR tip from Bruker (spring constant 40 N m^{-1}).

Reflectance Measurements: Reflection measurements (Figures 2b and 6b) were performed using a Nikon C2 confocal microscope. Unpolarized light from a halogen lamp illuminated the sample through a 50 × long working distance objective (Nikon LU Plan ELWD, numerical aperture (NA) = 0.6). Broadband wide-field illumination was used, with the aperture stop closed to obtain minimally focused excitation with angles of incidence close to normal. The reflection signal was collected by a confocal scanner with a 60-µm pinhole and analyzed using a SpectraPro 2300i spectrometer (150 lines mm−1, blazed for λ = 500 nm) and a Pixis Si charge-coupled device (CCD; −70 °C detector temperature). The final spectra were smoothed by a running average with a bin width of 3 pixels.

Diffraction Efficiency Experiments: The diffraction efficiency measurements were also performed using the Nikon C2 confocal microscope, equipped with a Bertrand lens to access the back-focal-plane of the same 50 × long working distance Nikon objective. A supercontinuum laser (NKT SuperK extreme EXW-12) coupled to an acousto-optical tunable filter (AOTF, SuperK select, ∼5 nm linewidth) was used to control the intensity and wavelength of the incident light. For top illumination, the laser was fiber-coupled to the microscope turret via a single-mode fiber. Images of the Fourier space were recorded using the same Pixis Si CCD. Please see Section S3 (Supporting Information) for an error analysis of the diffraction efficiency.

FDTD Simulations: The scattered-field simulations (Figure 4a), the effective reflection coefficient simulations (Figure 5a–d), as well as the first order diffraction efficiency simulations (Figure 6b,c; Figure S2b,d, Supporting Information) were obtained using finite-difference time-domain (FDTD) simulations (Ansys Lumerical Inc.). All simulations are 2D, with the grating period along the x-axis, light source propagating along the -y-axis, and polarization along the length of the grating's ribbons (electric field along the z-axis). Refractive indices of $n = 1.459$, $n = 1$, $n = 1.419$ for SiO_2, air, and DEME:TFSI were used, respectively. The WS_2 monolayer was modeled as a 2D conductance sheet with conductance derived from the refractive index of the material taken from literature.[22] For the scattering cross-section and phase of the scattered fields (Figure 4a) a total-field-scattered-field light source was used with perfectly matched layers boundary conditions in all directions. For the reflection coefficient simulations (Figure 5a,b), a plane-wave excitation was used with polarization along the length of the grating's ribbons (z-axis), perfectly matched layers boundary conditions for the y-axis, and periodic boundary conditions for the x-axis. Each ribbon size was stimulated individually in an FDTD box with width corresponding to the subperiod (sp = 300 nm). To extract the propagation phase, a calibration simulation was performed with the same settings, but

employing a perfect electrical conductor in place of our material stack. For the first order diffraction efficiency simulations (Figure 6b,c; Figure S2b,d, Supporting Information) the same source and boundary conditions were used as for the reflection coefficient. The whole grating period was simulated within a FDTD box with width coinciding with the period size (p = 2400 nm).

RCWA Simulations: The blazed grating reflection spectra were computed using the Fourier Modal Method using a freely available software package.[24] A 2D layer system was set up consisting of superstrate, grating layer, and substrate, with the blazed grating structure modeled as individual square blocks of a height of 0.618 nm and widths as described in Section S1 (Supporting Information), and the full lattice period repeated automatically. The dielectric function of the WS_2 monolayer blocks was given by a Lorentzian model with three oscillators and a constant offset, and the lateral permittivity distribution was subsequently transformed into reciprocal space via closed-form Fourier transform. Solving for the reflection and transmission amplitudes of all diffraction orders using 101 Fourier expansion orders, the reflected power per order was extracted, taking the added lattice momentum per order as well as the permittivity of the embedding media into account. For the results shown in Figure 1c–e, the first order diffraction efficiencies are normalized by the 0th order, with the incoherent reflection from the rear side of the quartz substrate accounted for in the 0th order to match the experiments (Figure 7c,d).

DFT Calculations: The semi-analytic DFT calculations for blazed amplitude and phase gratings assume a discrete amplitude and phase response at the grating layer, with the grating response set up by a 1D array with 100-pixel discretization and a lattice repetition of 1000. The far field response of such a structure was then extracted via direct Fourier transform of the response function, leading to the diffraction order intensity structures seen in the main manuscript. In case of a pure amplitude grating a fully analytic description can be obtained by using the series expansion of a sawtooth function as $f(x) = \frac{1}{2} - \frac{\sum_{n=-1}^{\infty} \sin(n\frac{2\pi x}{p})/n}{\pi}$ with p the period of the grating. Since only sine functions are used in this expansion (given by the odd symmetry of the sawtooth), equal intensity contributions exist for negative and positive spatial frequencies (albeit with π phase shift between them), leading to the fully symmetric intensity response of the grating orders.

Supporting Information

Supporting Information is available from the Wiley Online Library or from the author.

Acknowledgements

This work was funded by institutional funding of the University of Amsterdam. T.B. and J.v.d.G were also supported by a Vidi grant (VI.Vidi.203.027) from the Dutch National Science Foundation (NWO). The Brongersma group was funded by Department of Energy grant DE-FG02-07ER46426 and by a MURI program of the United States Air Force Office of Scientific Research (GrantNo. FA9550-21-1-0312). Preparation of monolayers at Stanford was supported by the Defense Advanced Research Projects Agency (DARPA) under Agreement No. HR00112390108. Part of this work was performed at the Nano@Stanford labs, supported by the National Science Foundation under award ECCS-1542152.

Conflict of Interest

The authors declare no conflict of interest.

Author Contributions

L.G., T.B., and J.v.d.G. conceived the concept behind this research. A.P.S. and F.L. performed the large-area exfoliation. L.G., T.B., and Q.L. fabricated the contacts and the gratings, J.H.S. fabricated the ionic liquid cell. S.S. wire-bonded the sample to the holder. L.G. performed the back-focal plane measurements with the help of Q.L. and J.H.S., and S.S. L.G. performed the scattered field analysis, T.B. performed the diffraction efficiency calculations. L.G. performed the data analysis, with input from T.B., J.v.d.G., and M.L.B. All authors contributed to writing the manuscript.

Data Availability Statement

The data that support the findings of this study are openly available in FigShare at https://doi.org/10.6084/m9.figshare.28746125, reference number [28746125].

Keywords

2D semiconductor, beam steering, exciton, metasurface, wavefront manipulation

Received: November 26, 2024
Revised: April 9, 2025
Published online:

[1] P. Berini, *ACS Photonics* **2022**, *9*, 2204.
[2] N. Yu, P. Genevet, M. A. Kats, F. Aieta, J.-P. Tetienne, F. Capasso, Z. Gaburro, *Science* **2011**, *334*, 333.
[3] D. Lin, P. Fan, E. Hasman, M. L. Brongersma, *Science* **2014**, *345*, 298.
[4] R. A. Aoni, M. Rahmani, L. Xu, K. Zangeneh Kamali, A. Komar, J. Yan, D. Neshev, A. E. Miroshnichenko, *Sci. Rep.* **2019**, *9*, 6510.
[5] S. Q. Li, X. Xu, R. M. Veetil, V. Valuckas, R. Paniagua-Domínguez, A. I. Kuznetsov, *Science* **2019**, *364*, 1087.
[6] G. K. Shirmanesh, R. Sokhoyan, P. C. Wu, H. A. Atwater, *ACS Nano* **2020**, *14*, 6912.
[7] C. R. de Galarreta, A. M. Alexeev, Y. Y. Au, M. Lopez-Garcia, M. Klemm, M. Cryan, J. Bertolotti, C. D. Wright, *Adv. Funct. Mater.* **2018**, *28*, 201704993.
[8] A. L. Holsteen, A. F. Cihan, M. L. Brongersma, *Science* **2019**, *365*, 257.
[9] J. van de Groep, J. H. Song, U. Celano, Q. Li, P. G. Kik, M. L. Brongersma, *Nat. Photonics* **2020**, *14*, 426.
[10] I. Epstein, B. Terrés, A. J. Chaves, V. V. Pusapati, D. A. Rhodes, B. Frank, V. Zimmermann, Y. Qin, K. Watanabe, T. Taniguchi, H. Giessen, S. Tongay, J. C. Hone, N. M. R. Peres, F. H. L. Koppens, *Nano Lett.* **2020**, *20*, 3545.
[11] M. L. Brongersma, *Nanophotonics* **2020**, *10*, 643.
[12] J. Lynch, L. Guarneri, D. Jariwala, J. van de Groep, *J. Appl. Phys.* **2022**, *132*, 091102.
[13] M. Li, C. U. Hail, S. Biswas, H. A. Atwater, *Nano Lett.* **2023**, *23*, 2771.
[14] P. Lalanne, S. Astilean, P. Chavel, E. Cambril, H. Launois, *Opt. Lett.* **1998**, *23*, 1081.
[15] W. Stork, N. Streibl, H. Haidner, P. Kipfer, *Opt. Lett.* **1991**, *16*, 1921.
[16] Y. Yu, Y. Yu, L. Huang, H. Peng, L. Xiong, L. Cao, *Nano Lett.* **2017**, *17*, 3613.
[17] F. Liu, W. Wu, Y. Bai, S. H. Chae, Q. Li, J. Wang, J. Hone, X. Y. Zhu, *Science* **2020**, *367*, 903.
[18] J. van de Groep, Q. Li, J.-H. Song, P. G. Kik, M. L. Brongersma, *Nanophotonics* **2023**, *12*, 3291.
[19] J. S. Ross, S. Wu, H. Yu, N. J. Ghimire, A. M. Jones, G. Aivazian, J. Yan, D. G. Mandrus, D. Xiao, W. Yao, X. Xu, *Nat. Commun.* **2013**, *4*, 1474.

[20] D. A. B. Miller, *Science* **2023**, *379*, 41.
[21] M. Li, S. Biswas, C. U. Hail, H. A. Atwater, *Nano Lett.* **2021**, *21*, 7602.
[22] L. Guarneri, Q. Li, T. Bauer, J. H. Song, A. P. Saunders, F. Liu, M. L. Brongersma, J. van de Groep, *Nano Lett.* **2024**, *24*, 6240.
[23] J. Lynch, P. Kumar, C. Chen, N. Trainor, S. Kumari, Y. Peng, C. Y. Chen, Y. Lu, J. Redwing, D. Jariwala, *Device* **2025**, *3*, 100639.
[24] V. Liu, S. Fan, *Comput. Phys. Commun.* **2012**, *183*, 2233.